International Journal for Multidisciplinary Research (IJFMR)
E-ISSN: 2582-2160 ● Website: www.ijfmr.com ● Email: editor@ijfmr.com

# Efficient Deep Learning Analysis of Retinal Images for Diabetic Eye Disease Screening

**Mr. Pothula Nani Babu**

M Tech (PhD), Assistant Professor, VSM College of Engineering(A), Ramachandrapuram.

**Abstract:**
Diabetic retinopathy (DR), diabetic macular edema (DME), and glaucoma are among the various eye conditions that diabetes individuals are susceptible to. Glaucoma affects the optic disk and results in vision loss in its advanced stages, while DR damages the retina and DME is caused by fluid buildup in the macula. But because the disease progresses slowly, it does not display many symptoms in its early stages, which makes it hard to detect. Therefore, to help the early stages of detection and screening, a fully automated system is needed. This study presents an automated method for disease localization and segmentation using fuzzy k-means (FKM) clustering and the Fast Region-based Convolutional Neural Network (FRCNN) algorithm. Since the FRCNN is an object detection method that depends on bounding-box annotations to function, we have created these annotations using ground-truths because datasets do not supply them. The annotated images are then split out using FKM clustering, and FRCNN is trained over them for localization. Intersection-over-union operations are then used to compare the segmented regions to the ground facts. We employed the Diaretdb1, MESSIDOR, ORIGA, DR-HAGIS, and HRF datasets to assess performance. The effectiveness of the strategy in terms of disease identification and segmentation is confirmed by a thorough comparison with the most recent techniques.

**Keywords:** fuzzy K-means clustering, diabetic retinopathy, glaucoma, deep learning, and medical imaging

## 1 Introduction:

An very high blood sugar level is a symptom of diabetes. Various eye conditions, such as diabetic retinopathy (DR) [1], diabetic macular edema (DME) [2], and glaucoma [3], can cause victims to lose their vision entirely. The primary symptoms of DR, a condition that harms the retina, include impaired vision, floaters, and abrupt visual loss. The abnormality symptoms of DR include microaneurysms, hemorrhages, and hard and soft exudates [4]. The formation of hard exudates, which are waxy, bright yellow patches on the retina, is caused by blood leaking from arteries. Occlusion of the arteriole causes white lesions on the retina called soft exudates. Hemorrhages are dark red patches that form as blood leaks from broken arteries. Microaneurysms, which manifest as tiny red spots on the retina, are caused by abnormalities in the blood vessel's border. Another eye condition that can induce vision loss in patients who already have DR is DME. Blindness can happen at any stage of DR, although it is more likely to happen later as the disease worsens. Other medical disorders brought on by inadequate blood sugar control raise the risk of blindness for individuals with DME. The macula, the center portion of the retina responsible for central vision, swells as a result of DME-induced fluid buildup in the macula

region. Any injury to the macula region results in loss of central vision. If left untreated, DME frequently manifests as blurred vision, double vision, floaters, and blindness [5].

About 80 million people worldwide are thought to be affected by glaucoma, an eye condition that destroys the optic disk (OD) and optic cup (OC) and results in advanced stages of vision loss [6,7]. Disk size, cup to disc ratio (CDR), neuroretina rim ratio in the inferior, superior, nasal, and temporal quadrants, peripapillary atrophy, and other fundamental structural glaucoma indicators are usually concentrated on the OD. OC is the center component of OD, which is the morphological structure visible in the cross-sectional view of the optic nerve connecting to the retina. Because of the imbalance in intraocular pressure (IOP) within the eye, glaucoma affects the optic nerve. The retinal layer is weakened by the damaged nerve fibers, raising the CDR. IOP measurement, a patient's medical history, visual field loss testing, and visual examination of the disease using ophthalmoscopy to examine the color, size, and shape of the optic nerve are the standard methods used to diagnose eye diseases [8]. Handcrafted features have been employed to distinguish between affected and normal portions of the images in order to automatically detect eye disorders [11–25]. However, due to factors including color, size, greater intra-class fluctuations, and light regions other than OD, these features are unable to accurately represent the DR, DME, and glaucoma regions, which leads to unsatisfactory CAD solution results [26]. Glaucoma classification is carried out using an appropriately divided CAD system for performance optimization. For DR detection [14,15,27,28], classification, DME detection [2,5,29–31], and glaucoma sign identification from retinal pictures [32–39], a variety of computer vision and deep learning-based techniques were used. Table 1 summarizes a review of the literature on key techniques for DR, DME, and glaucoma detection.

**Table 1: Methods for diabetes-related ocular problems are compared.**

| Reference | Method | Findings | Shortcomings |
|---|---|---|---|
| Pan et al. [15] | The model is based on DenseNet, ResNet50, and VGG16 models. | Detection of DR lesions and the method is computationally robust. | The method may not classify microaneurysms efficiently because these are easily misclassified under the pervading presence of fluorescein. |
| Zeng et al. [28] | A Siamese-like CNN framework by employing the concept of weigh-sharing layers based on Inception V3. | The work exhibits promising results for DR prediction with kappa score of 0.829. | It may not perform well for those sample databases where paired fundus images are not available. |
| Qummar et al. [14] | Five different frameworks of CNN named Dense169, Inception V3, Resnet50, Dense121, and Xception were employed. | To locate and classify the DR lesions into different classes according to the severity level of moles. | The method suffers from high computational cost. |

| | | | |
|---|---|---|---|
| Zhang et al. [40] | A DL framework named DeepDR was presented for DR detection. In addition, a new database for DR labelled DR images was also introduced. | The proposed network has attained the sensitivity value of 97.5%, along with the specificity value of 97.7%. | The introduced model needs to be evaluated on more complex and larger datasets. |
| Torre et al. [41] | A DL based method was used to predict the expected DR class and assign scores to individual pixels to exhibit their relevance in each input sample. The assigned score was employed to take final classification decision. | The introduced DL framework acquired more than 90% of sensitivity and specificity values. | The evaluation performance of the presented algorithm can be improved through appropriate measures. |
| Rekhi et al. [2] | The method was based on geometrical, morphological, and orientation features. The classification was performed through SVM. | Grading and classification of DME from fundus images with an accuracy of 92.11%. | The detection accuracy needs further improvement. |
| Kunwar et al. [5] | The method was based on texture features and the SVM classifier. | High-risk DME detection with accuracy of 86%. | Experiments were performed on a small dataset. |
| Marin et al. [30] | The method was based on thresholding and regularized regression techniques. | DME risk detection with 0.90 sensitivity. | The detection performance requires improvement. |
| Perdomo et al. [31] | The presented method was composed of two-stage CNNs. | The method detects regions of interest in the retinal image and then predicts its class of DME. | The technique is computationally complex. |
| Jiang et al. [32] | The end-to-end Region-based Convolutional Neural Network was used for OD and OC segmentation. | OD and OC segmentation with AUC of 0.901. The method is robust to glaucoma detection. | The method is computationally complex because it employs two separate RCNNs to compute the bboxes of the OC and OD, respectively. |
| Bajwa et al. [37] | The localization was achieved through RCNN, while the other stage used deep CNN to classify the computed disc into glaucomatous or healthy. | Localization and classification of glaucoma with AUC of 0.874. | The method is computationally complex as it takes a two-stage framework to localize and classify the glaucoma. The performance is affected by increasing the network hierarchy as it results in losing the discriminative set of |

| | | | |
|---|---|---|---|
| | | | features. |
| Zheng Lu et al. [38] | The Modified U-Net model was improved by minimizing the original U-shape structure through adding 2-dimensional convolutional layer. | Before OD segmentation, the ground-truths were generated through the GrabCut method. | The presented technique requires less training, however, shows lower segmentation accuracy as compared to latest approaches because of missing ground truths. |
| Ramani et al. [39] | The region-based pixel density calculation method based on Circular Hough Transform with Hough Peak Value Selection and Red Channel Super-pixel method. | The technique is robust and efficient for optic disc segmentation. | The detection accuracy is affected over the images having pathological distractions. |

We describe a deep learning (DL) method in the work that identifies the bounding boxes (bboxes) of disease locations. Lastly, we partition the localized sections rather than the entire image. This method is efficient in terms of complexity and time consumption, as demonstrated by experiments. The suggested approach is predicated on FKM and FRCNN clustering. Our suggested approach uses supervised fine-tuning regions for localization and unsupervised pre-training to address the issue of inadequate samples. A single-stage training method called FRCNN is used to categorize region proposals and improve their localization. The softmax layer then correctly classifies the areas after FRCNN generates some class-independent region proposals of images and uses a CNN to extract a fixed-size feature descriptor from each proposal.

## 2. Suggested Approach:

Fundus image-based diabetes-based eye disease detection is regarded as a two-way process. The first phase is identifying and locating the disease, and the second is using FKM clustering to segment the localized sections. We apply the FRCNN method in the localization step. As an input to the group and bbox regression fully connected layer, we create the annotations for three diseases, which are then sent to the FRCNN training, which takes the features out of the images and sends them to the ROI pooling layer. The test photos are used to pinpoint the affected areas and assign a regression confidence score to the model. Finally, FKM clustering—which is regarded as a reliable technique—is used for the segmentation.

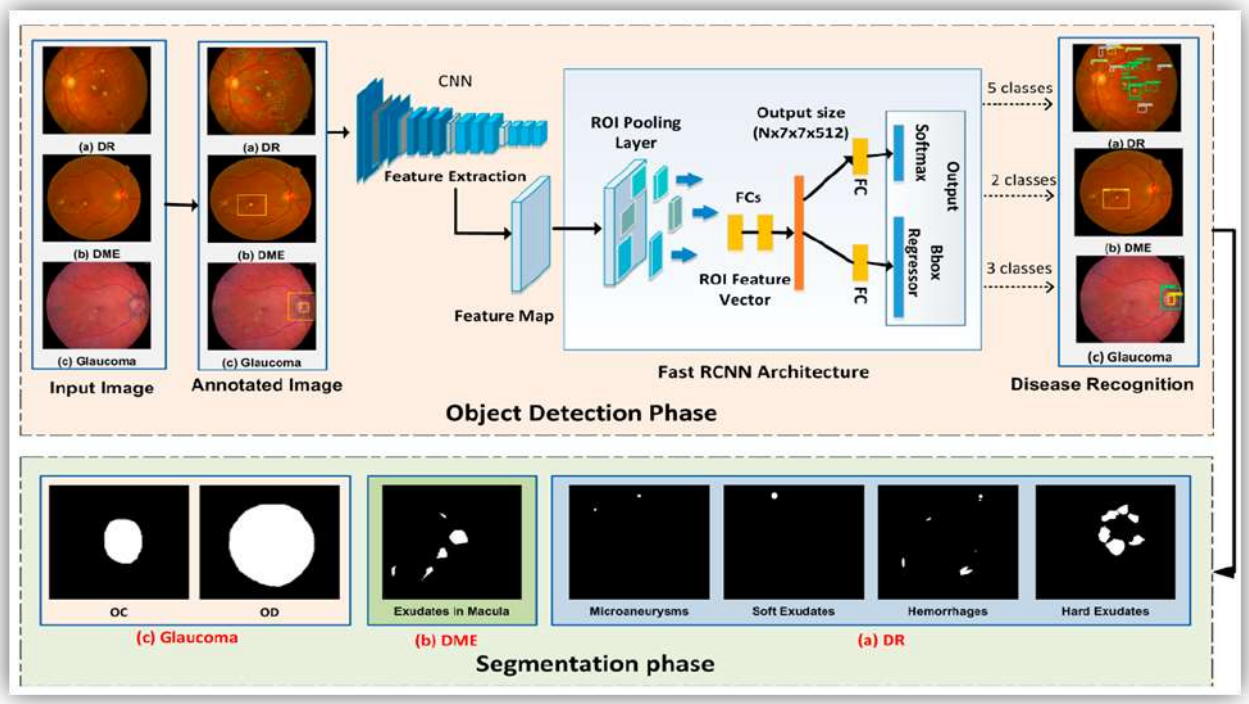


**Figure 1** :

shows the suggested method's framework. FRCNN is used to find the ROI for the disease in question during the object detection phase. Using FKM clustering, the identified areas of each of the three diseases are separated out during the segmentation step.

### 2.1 Generating Ground Truth:

For the training procedure, the affected region must be identified using the ground-truth bbox against each image. The retinal images are annotated using the LabelImg [42] program, and each image's bbox is manually created. An example of an original image and its matching ground truth image are displayed in Figure 2. The annotations, which include the object's class and its bbox values (xmin, ymin, xmax, ymax, width, and height), are stored in.xml files. For every image, an XML file is generated. These files are then used to generate a CSV file, from which a train.record file is generated. This CSV file is then utilized in the training procedure.

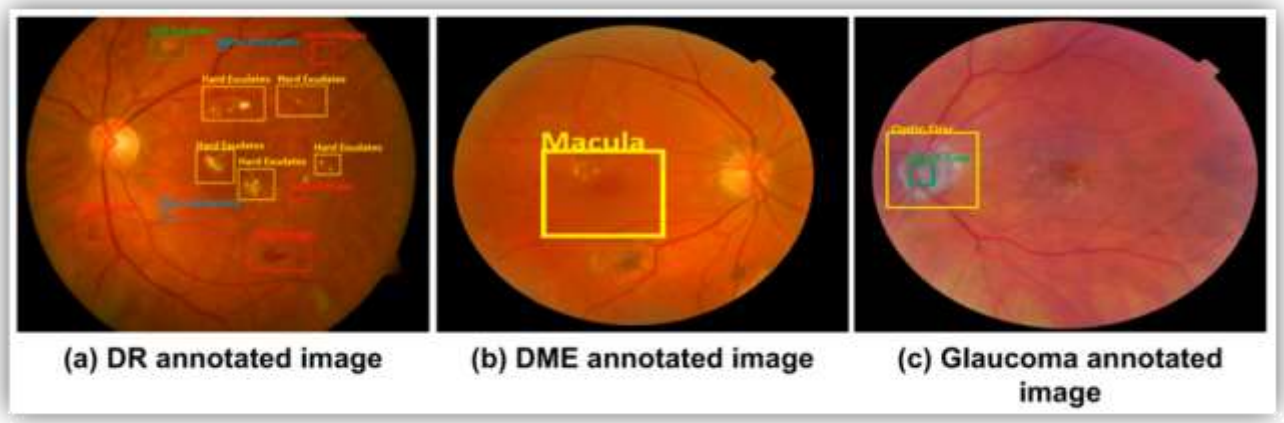

Figure 2 shows sample photos with annotations for each of the three disorders. The picture annotations for DR indications and objects, such as microaneurysms, soft exudates, hard exudates, and hemorrhages, are shown in (a). The DME indication is shown by (b) (macula). (c) shows the OC and OD image annotations for glaucoma.

As seen in Error!, we have created annotations for three diseases based on their symptoms. No reference source could be located. Microaneurysms, soft exudates, hard exudates, hemorrhages, and background are the five classes present in the DR-affected picture, while DME has two classes: DME and background. The three classes of glaucoma, the third illness, are O

| DR | DME | Glaucoma |
|---|---|---|
| 0. Background | 0. Background | 0. Background |
| 1. Microaneurysms | 1. Macula Region | 1. OD |
| 2. Soft Exudates | | 2. OC |
| 3. Hard Exudates | | |
| 4. Hemorrhages | | |

**2.2 Localization Phase:**

Because the tasks are the same—that is, to locate objects—the method used stays the same. The only distinction is that each of the three diseases has a different number of classes.

**2.2.1. Localization of DR Regions:**

The region proposals and the photos are sent into the FRCNN. Our approach examines the entire image and generates the Conv feature map using max-pooling and convolutional (Conv) layers. The ROI pooling layer is used to obtain fixed-size feature vectors from the Conv feature map. Before branching into distinct output layers, it is fed into a sequence of fully connected (fc) layers. The first layer calculates Soft max-probability estimates over k = 5 region classes, and the second layer generates four real-valued numbers for five region classes, each of which represents a position of the bbox for one of the five classes [43]. Using FRCNN, we trained the multi-class DR object identification model, which is capable of precisely localizing multiclass items from an image. Four plus one classes—hemorrhages, microaneurysms, soft and hard exudates, and one background class—are available for DR localization.

**2.2.2. Localization of DME Region:**

We have utilized FRCNN to locate the macula region from retinal images. FRCNN may be trained to locate binary class objects. The background and macula regions, which are represented by 0 or 1, are the two region classes in this instance. The macula is represented by the area inside the bbox, while the background is the remaining area of the picture. The entire image is processed using the max-pooling and convolution layers to create the feature map. The ROI pooling layer is used to obtain fixed-size feature vectors from the Conv feature map. The first layer calculates softmax-probability estimates over k = 2 region classes, and the second layer generates four real-valued numbers for two region classes of DME, each of which represents a position of the bbox for one of the DME classes. The data is then fed into a sequence of fc layers before branching into distinct output layers.

**2.2.3. Glaucoma Region Localization:**

We have trained our method for three classes—OD, OC, and background—in order to detect the third eye ailment, glaucoma. The OD and OC regions were localized by FRCNN, and the remaining retinal picture is regarded as background. The ROI pooling layer is used to extract fixed-size feature vectors

from the Conv feature map, which is created by the max-pooling and Conv layers. The first layer calculates Softmax-probability estimates over k = 3 region classes, and the second layer generates four real-valued numbers for three region classes that represent a position of the box for one of the glaucoma classes. The data is then fed into a sequence of fc layers before branching into distinct output layers.

**The extraction of features:**

To locate the region of interest—that is, cars, buildings, etc.—object localization techniques use a sliding window. Nevertheless, breakthroughs in deep learning techniques like CNN have effectively supplanted older detection methods. To increase performance, FRCNN suggests regions using a selective search approach, which can train all network weights with backpropagation. These methods, however, are economically costly because they only use the sliding window method for object localization. The CNN network initializes FRCNN and goes through three conversions:

(i) The RoI layer replaces the max-pooling layer for VGG16 with h = w = 7.

(ii) Two sister output layers, the f c and Softmax over the k + 1 category, are created in place of the f c and softmax layers.

(iii) The list of pictures I(x,y) and the list of ROIs from the input images are the two inputs required by our suggested technique [45].

**Loss of Multiple Tasks:**

FRCNN is an end-to-end learning framework that learns the region class and associated bbox position and size using a multi-task loss function. Class name u and bbox regression target v are assigned to each ROI. Let t be the outcome of the regressor sibling layer, which is the bbox tuple for each class k, and let p be the output of the Softmax sibling layer, which is the probability distribution over k classes including background class [46]. Equation (1) illustrates how we jointly trained for classification loss and bbox regression loss using a multi-task loss L on each labeled ROI:

$$L(p, u, t^u, v) = L_{cls}(p, u) + \lambda[u \geq 1] L_{loc}(t^u, v)$$

$$L_{loc}(t^u, v) = \sum_{i \in \{x,y,w,h\}} S_{L1}(t_i^u - v_i)$$

$$S_{L1}(x) = \begin{cases} 0.5x^2 & if\ |x| < 1 \\ |x| - 0.5 & otherwise \end{cases}$$

The hypermeter represented by ` in Equation (1) ,λ establishes the relative importance of the regression loss compared to the classification loss in relation to the total loss. For all of the experiments, we used λ = 1. There is no Lloc declared for the background class, as indicated by the [u > = 1]. The distance between vectors is denoted by x in Equation (3). The derivatives are sent by the RoI pooling layer using backpropagation, as described in [47].

### 2.3 Region Segmentation Using Fuzzy K-Means Clustering:

To find the precise border of the affected zone, the localized regions are chopped using computed coordinates. We have segmented the regions of three eye illnesses using the fuzzy k-means (FKM) technique independently. The localized regions are segmented independently in the case of DR segmentation. The value of the other portion is set to zero, which indicates black, while the localized regions are set to foreground. Likewise, the FKM clustering approach is used to segment the localized macular region.

$$L = \sum_{j=1}^{k} \sum_{i=1}^{N} b_{i,j}^{f} g_{i,j}$$

$$b(i,j) = ((g_{(i,j)}{}^{(1/m-1)} \sum_{l=1}^{k} (\frac{1}{g_{il}})^{\frac{1}{m}-1}))^{-1}$$

$$C_j(p) = \frac{\sum_{j=1}^{N} b_{i,j}{}^{m} X_i}{\sum_{j=1}^{N} b_{i,j}{}^{m}}$$

## 3. Results of the Experiment:

### 3.1. Information Sources:

Since the five open source databases we used in our eye illness detection experiments (Diaretdb1, MESSIDOR, HRF, DRHAGIS, and ORIGA) lacked bbox ground truths, we first created the bbox annotations of the datasets that are required for the FRCNN training. The dataset used to benchmark DR detection from retinal pictures is Diaretdb1 [51].
Of the 89 fundus samples in the Diaretdb1 database, 84 photographs show DR signals, whereas the five other samples are regarded as normal, meaning they show no evidence of DR. The following symptoms are indicative of DR lesions: hard and soft exudates, microaneurysms, and haemorrhages. The pictures, which have a resolution of 1500 by 1125 pixels, were captured using a fundus camera with various image settings and the same 50-degree field-of-view (FOV). There are 1,200 photos with the grades DR and DME in the MESSIDOR database. A 3CCD camera with a 45-degree field of view with resolutions of 2304 x 1536, 2240 x 1488, and 1440 x 960 pixels was used to take the pictures.

### 3.2. Metrics for Evaluation:

We have taken into consideration the following evaluation indicators in order to assess the effectiveness of our suggested technique:

$$IoU = \frac{TP}{FN + FP + TP} \times 2$$

We iterate over test photos according to precision in order to determine the average precision (AP). The mean average precision (mAP) is shown by equation (8):

$$mAP := \sum_{i=1}^{T} AP(t_i)/T$$

In this case, AP($t_i$) is the average precision for the specified test image category, and T is the number of test photos.

We have used the following metrics as evaluations for segmentation: specificity (SP), sensitivity (SE), area under the curve (AUC), accuracy (Acc), and dice coefficient (Dc):

$$D_c = \frac{2 \times TP}{2 \times TP + FN + FP}$$

**3.3. Results:**

This section presents the outcomes of the suggested method and compares the given methodology with the most recent methods.

**3.3.1. FRCNN Evaluation:**

We compared FRCNN's assessment power to other methods, such as RCNN [56] and SPPnet [44], which employ bbox regression and a comparable pre-trained framework. FRCNN employs single scale testing and training, whereas SPPnet uses five scales. Although the RCNN approach uses a deep ConvNet to attain outstanding performance, it has certain drawbacks: For example, object detection is sluggish, ConvNet to SVMs to bbox regressors are costly in terms of time and space, and training is costly.

**Table 3: Evaluation of the proposed technique's performance in comparison to alternative methods**

| A | B |
|---|---|
| **Technique** | **mAP** |
| **SPPnet [44]** | **0.85** |
| **RCNN [56]** | **0.89** |
| **FRCNN (Proposed)** | **0.94** |

**3.3.2. DR Region Localization:**

The affected areas are regarded as positive examples for the localization of the DR symptoms (hemorrhages, microaneurysms, hard and soft exudates), whereas the background and other portions are regarded as negative examples. The overlapped area is designated as background when the threshold value IoU is less than 0.3.

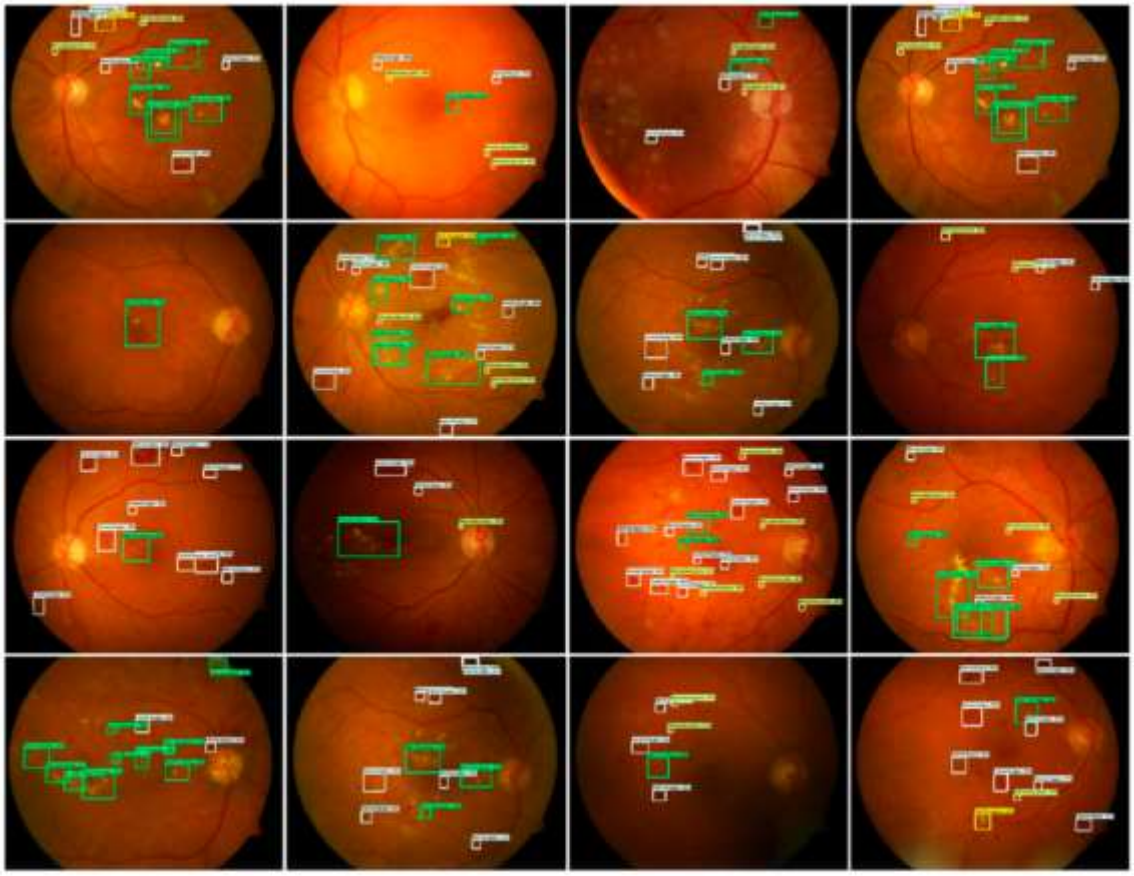

**Figure 3: Dr.'s test results**

### 3.3.3. DME Region Localization:

We have used the MESSIDOR dataset to assess the performance of DME identification from retinal pictures. The macula region was precisely identified using FRCNN, and the normal and DMEaected regions were classified by the Softmax layer. Figure 4 displays the visualization results of DME localization. With a mean average precision of 0.943, FRCNN located the macular edema location at the regressor layer.

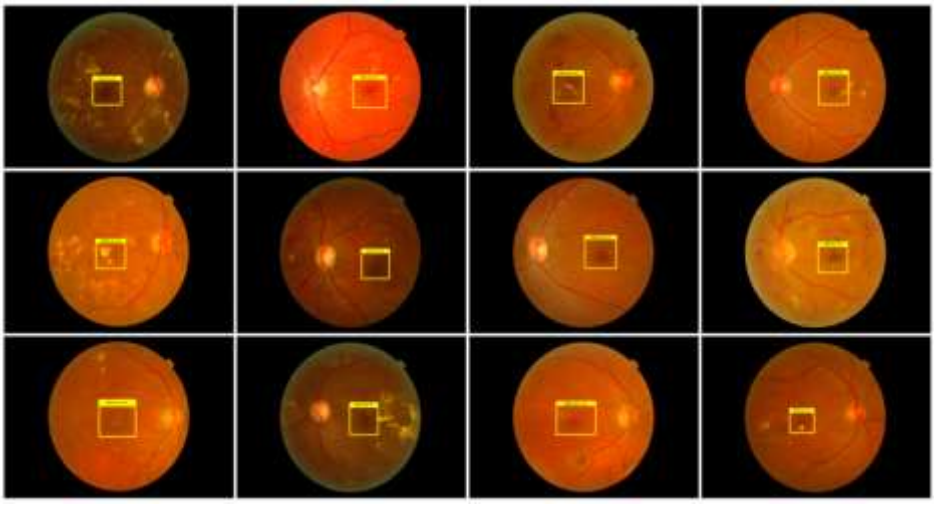

**Figure 4. Test results of DME**

### 3.3.4. Localization of Glaucoma Regions:

To locate glaucoma, we used the FRCNN approach. RPN creates multiple random rectangular area recommendations with corresponding region ratings based on an image of the glaucoma region. Figure 5 displays the FRCNN's glaucoma localization result using 35 test pictures from three datasets. A higher score—more than 0.84 and up to 0.94—is displayed in the test results. Table 4 reports the accuracy of glaucoma localization on three datasets: HRF, DR-HAGIS, and OR. IGA With a mAP of 0.940 across all datasets, we can assert that our approach can precisely locate the glaucoma areas.

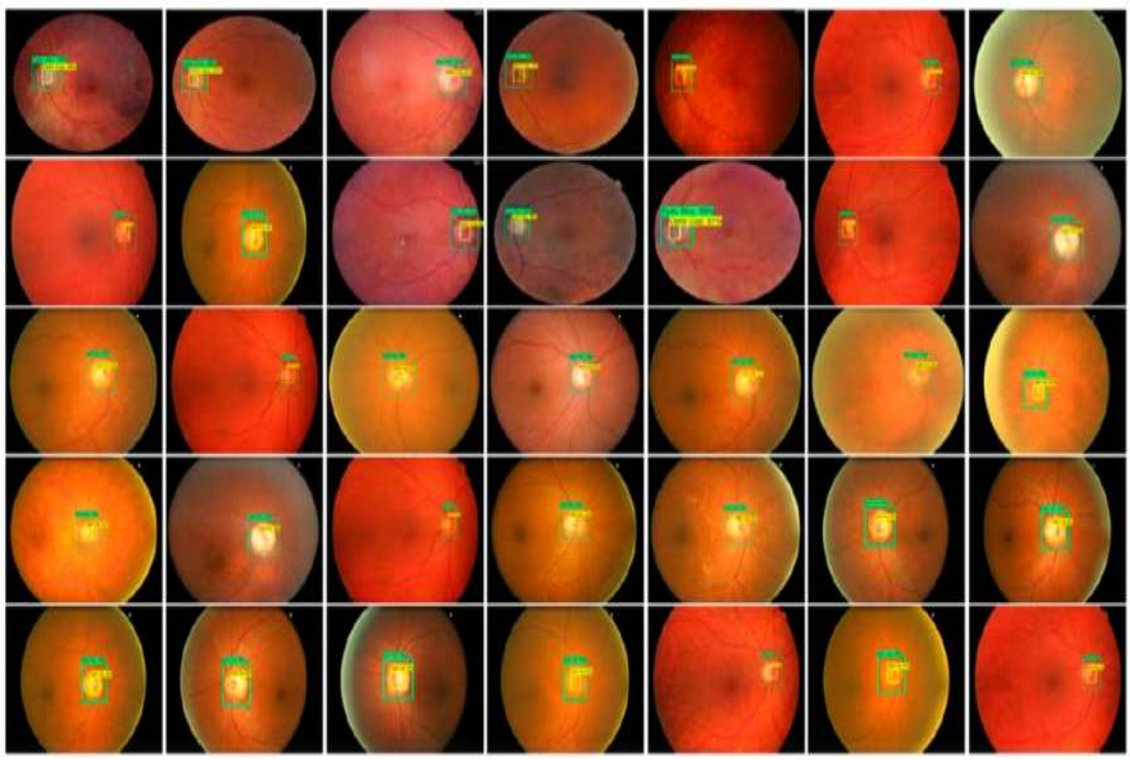

**Figure 5: Test image localization results.**

**Table 4. Glaucoma results.**

| Dataset | Img1 | Img2 | Img3 | Img4 | Img5 | Img6 | Img7 | Img8 | mAP |
|---|---|---|---|---|---|---|---|---|---|
| **HRF** | 0.95 | 0.94 | 0.96 | 0.94 | 0.99 | 0.89 | 0.95 | 0.94 | 0.95 |
| **DR HAGIS** | 0.94 | 0.94 | 0.98 | 0.89 | 0.91 | 0.94 | 0.99 | 0.93 | 0.94 |
| **ORIGA** | 0.94 | 0.94 | 0.9 | 0.88 | 0.97 | 0.99 | 0.94 | 0.95 | 0.94 |

### 3.3.5. Results of Segmentation:

In addition to producing an economically viable low dimensional initial sample, extracting the localization of the affected parts allows deep neural networks to highlight the important areas of the image. Figure 6 displays the pixel-by-pixel segmentation results of the DR indications. The FRCNN approach is used to localize each of the four distinct indications of DR. Next, a comparison is made between the segmented and ground truth images. The SE, SP, and Acc for each image in the test dataset

are used to assess the results of the suggested technique. According to Table 5, the suggested method achieved average SE, SP, and Acc scores of 0.961, 0.965, and 0.952, respectively.

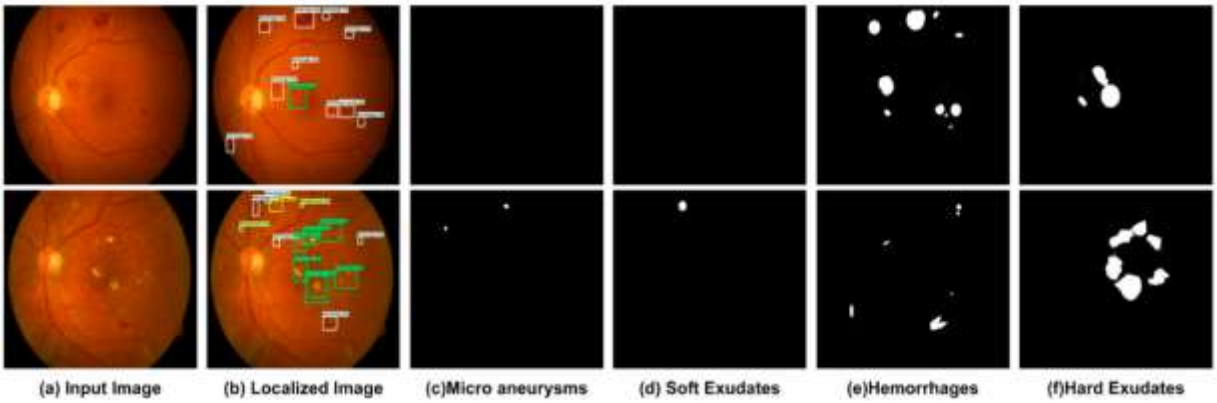


**Figure 6: DR sign segmentation results.**

**Table 5. Performance of Proposed method over Diaredb1 database.**

| DR Signs | Acc | SP | SE |
|---|---|---|---|
| Hard Exudates | 0.958 | 0.941 | 0.957 |
| Soft Exudates | 0.943 | 0.961 | 0.955 |
| Micro aneurysms | 0.957 | 0.954 | 0.943 |
| Hemorrhages | 0.952 | 0.96 | 0.951 1 |

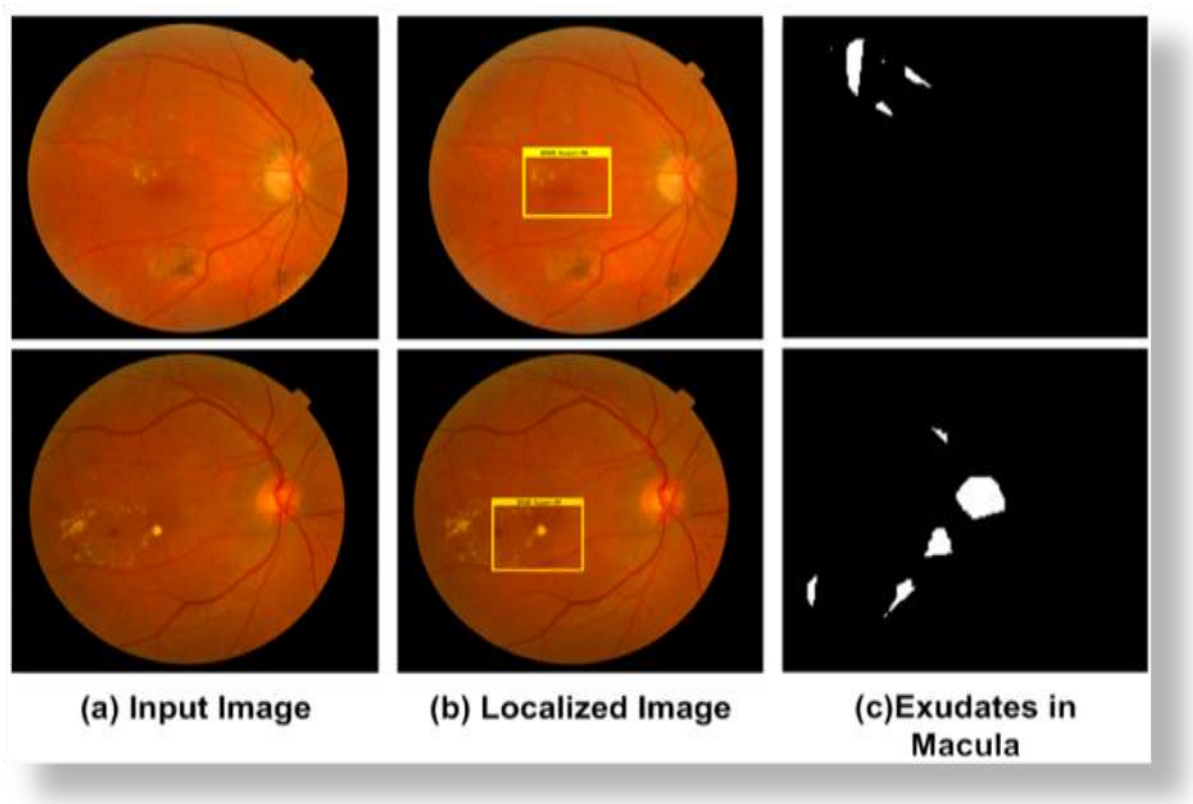


**Figure 7. Results of DME segmentation.**

The segmentation outcomes of the glaucoma regions of three datasets are shown in Figure 8. The suggested method achieved average values of SE of 0.951, SP of 0.961, Acc of 0.952, and Di of 0.928, as shown in Table 6. The precise localization of the OD and OC regions using FRCNN allowed the suggested technique to function well. However, for the reasons listed below, FRCNN identified the spurious OD regions in a small number of photos (as seen in Figure 9): (i) OD's apparent resemblance to brighter areas. (ii) Is unable to identify the OC in regions with low intensity.

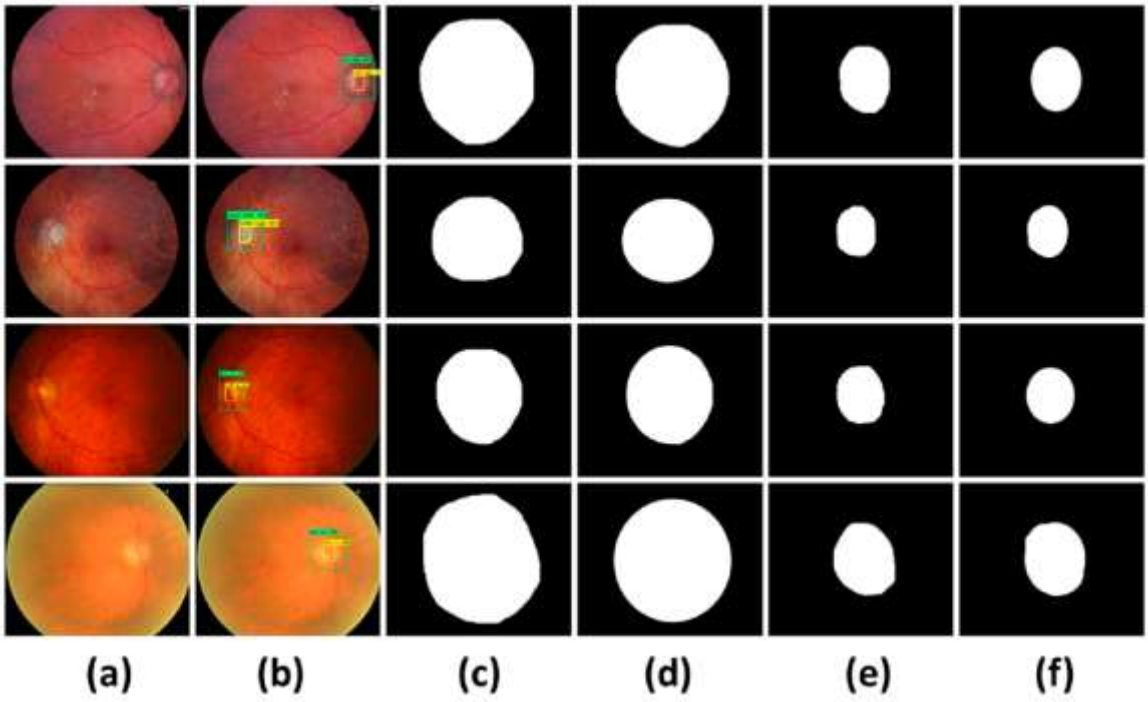


**Figure 8: Division Findings**
**(a). input pictures, (b). regional photos, (c). segmentation of OD, (d). Ground truths for OD, (e). OC division, as well as (f). OC ground realities.**

**Table 6 shows the suggested method's performance across three databases.**

| Database | Acc | Dc | SP | SE |
|---|---|---|---|---|
| **HRF** | 0.958 | 0.952 | 0.97 | 0.957 |
| **DR HAGIS** | 0.943 | 0.89 | 0.961 | 0.955 |
| **ORIGA** | 0.957 | 0.943 | 0.954 | 0.943 |
| **Average** | 0.9526 | 0.9283 | 0.961 | 0.951 |

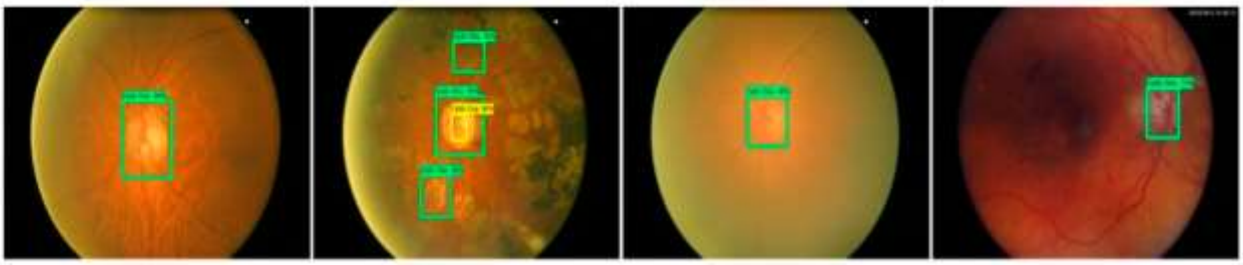

**Figure 9. Results of false detection.**

### 3.4. Studies of Comparison:

This section compares our approach to state-of-the-art techniques for the identification of glaucoma, DME, and DR. It is evident from the results that our approach had the highest accuracy of all of the approaches evaluated, at 95%.

**Table 7. Performance comparison against DR detection methods.**

| Technique | SP | SE | Acc | AUC |
|---|---|---|---|---|
| Zeng et al. [28] | 0.635 | 0.77 | - | 0.94 |
| Gulshan et al. [57] | 0.91 | - | 0.913 | 0.96 |
| Zhou et al. [58] | 0.863 | 0.995 | - | - |
| Kaur et al. [59] | 0.96 | 0.88 | 0.93 | - |
| Colomer et al. [61] | 0.818 | 0.81 | 0.93 | 0.92 |
| Abbas et al. [60] | 0.94 | 0.92 | - | 0.92 |
| Proposed | 0.965 | 0.961 | 0.95 | 0.967 |

Using the MESSIDOR dataset, we have evaluated our approach for DME identification against the works of Li et al. [62], Deepak et al. [63], Medhi et al. [64], Rekhi et al. [2], Lim et al. [65], Rahim et al. [66], Syed et al. [67], Varadrajan et al. [68], and Xiaodong et al. [69]. The comparison's findings are shown in Table 8. Our approach has a sensitivity SE of 0.96, which is comparable to Syed's approach.

**Table 8 compares the MESSIDOR dataset's performance to DME detection techniques.**

| Method | SE | SP | Acc |
|---|---|---|---|
| Li et al. [62] | 0.70 | 0.76 | 0.912 |
| Deepak et al. [63] | 0.95 | 0.90 | - |
| Medhi et al. [64] | 0.95 | 0.95 | - |
| Rekhi et al. [2] | - | - | 0.921 |
| Lim et al. [65] | 0.80 | 0.90 | - |
| Rahim et al. [66] | 0.85 | 0.55 | - |
| Syed et al. [67] | 0.96 | 0.95 | 0.935 |
| Varadarajan et al.[68] | 0.85 | 0.80 | - |
| Xiaodong et al. [69] | 0.959 | 0.97 | - |
| Proposed | 0.96 | 0.958 | 0.958 |

The works of Liao et al. [70], Chen et al. [71], Xu et al. [72], Li et al. [73], Bajwa et al. [37], Ramani et al. [39], Parakash et al. [74], and Krishna et al. [12] were compared to our approach for glaucoma identification. Table 9 presents the comparison findings utilizing the ORIGA, HRF, and DR HAGIS datasets.

**Table 9: Performance comparison between the suggested method and the most recent approaches**

| Method | Year | Dataset | SE | SP | AUC | Dc | Time |
|---|---|---|---|---|---|---|---|
| Liao et al. [70] | 2019 | ORIGA | - | - | 0.88 | 0.9 | - |
| Chen et al. [71] | 2015 | ORIGA | - | - | 0.838 | - | - |
| Xu et al. [72] | 2013 | ORIGA | 0.58 | - | 0.823 | - | - |

| | | | | | | | |
|---|---|---|---|---|---|---|---|
| Li et al. [73] | 2016 | ORIGA | - | - | 0.8384 | - | - |
| Bajwa et al. [37] | 2019 | ORIGA | 0.71 | - | 0.868 | - | - |
| Ramani et al. [39] | 2020 | HRF | 0.849 | 0.999 | - | - | 1.49 s |
| N.B Parakash et al.[74] | 2017 | HRF | 0.7025 | 0.997 | - | - | - |
| Krishna et al. [12] | 2019 | DR HAGIS | 0.94 | - | - | - | - |
| Proposed | - | ORIGA | 0.941 | 0.945 | 0.94 | 0.943 | 0.9 s |
| Proposed | - | HRF | 0.95 | 0.96 | 0.963 | 0.952 | 0.9 s |
| Proposed | - | DR HAGIS | 0.945 | 0.941 | 0.94 | 0.89 | 0.9 s |

Our approach outperformed the work of Ramani et al. [39] by around 10% in terms of SE over HRF dataset, while it outperformed the work of Parakash et al. [74] by about 24%.

## 4. Conversation:

Our primary contribution is the presentation of a consolidated model to target three eye diseases, namely diabetic retinopathy, diabetic macular edema, and glaucoma. In localization, the suggested model achieved mAP of 0.945, 0.943, and 0.941 for DR, DME, and glaucoma, respectively. We have used the af RCNN technique for the localization and recognition of the diabetes-based eye diseases. Our method is based on fast RCNN and fuzzy k-means clustering. FRCNN trains the model using a multi-task loss, adds the bbox regression and classification head, and uses backpropagation estimation. The suggested approach uses FRCNN to simultaneously identify the abnormalities of DR, DME, and glaucoma regions. Finally, FKM clustering accurately recovers the regions from localized regions. Our segmentation accuracy for the DR, DME, and glaucoma regions is 0.952, 0.958, and 0.9526, respectively. Furthermore, a model that is optimized for one disease might perform poorly for another. But with this work, we have dispelled this myth and developed a reliable method in the form of a model that has a very high accuracy rate in detecting and identifying three distinct eye disorders.

## 5. Final Thoughts:

A novel approach based on FRCNN with FKM clustering is put forth in the study that is being presented for the automated localization and identification of diabetes-related eye disorders, such as glaucoma, DR, and DME, in retinal pictures. The two stages of the suggested method are the segmentation of the localized regions using FKM clustering and the illness detection and localization phase.

Compared to the most recent methods, the FRCNN technique improves segmentation performance and can extract deep features with an optimum representation of eye illnesses. The findings show that the suggested treatment for three disorders produced a mean IoU of 0.95 and a mAP value greater than 0.94. Furthermore, the many segmentation challenges in medical imaging can also be resolved using our suggested method. In the future, the research will be expanded to include other retinal imaging disorders, such as cataracts and age-related macular edema degeneration.

## References:

1 Mateen, M.;Wen, J.; Hassan, M.; Nasrullah, N.; Sun, S.; Hayat, S. Automatic Detection of Diabetic Retinopathy: A Review on Datasets, Methods and Evaluation Metrics. IEEE Access **2020**, 8, 48784–

48811. [CrossRef]
2 Rekhi, R.S.; Issac, A.; Dutta, M.K. Automated detection and grading of diabetic macular edema from digital colour fundus images. In Proceedings of the 2017 4th IEEE Uttar Pradesh Section International Conference on Electrical, Computer and Electronics (UPCON), Mathura, India, 26–28 October 2017; pp. 482–486.
3 Al-Bander, B.; Al-Nuaimy, W.; Al-Taee, M.A.; Zheng, Y. Automated glaucoma diagnosis using deep learning approach. In Proceedings of the 2017 14th International Multi-Conference on Systems, Signals & Devices (SSD), Marrakech, Morocco, 28–31 March 2017; pp. 207–210.
4 Zago, G.; Andreão, R.V.; Dorizzi, B.; Salles, E.O.T. Diabetic retinopathy detection using red lesion localization and convolutional neural networks. Comput. Biol. Med. **2020**, 116, 103537. [CrossRef] [PubMed]
5 Kunwar, A.; Magotra, S.; Sarathi, M.P. Detection of high-risk macular edema using texture features and classification using SVM classifier. In Proceedings of the 2015 International Conference on Advances in Computing, Communications, and Informatics (ICACCI), Kochi, India, 10–13 August 2015; pp. 2285–2289.
6 Quigley, H.; Broman, A.T. The number of people with glaucoma worldwide in 2010 and 2020. Br. J. Ophthalmol. **2006**, 90, 262–267. [CrossRef]
7 Bourne, R.R.; Flaxman, S.R.; Braithwaite, T.; Cicinelli, M.V.; Das, A.; Jonas, J.B.; Kee_e, J.; Kempen, J.H.; Leasher, J.; Limburg, H.; et al. Magnitude, temporal trends, and projections of the global prevalence of blindness and distance and near vision impairment: A systematic review and meta-analysis. Lancet Glob. Health **2017**, 5, e888–e897. [CrossRef]
8 Al-Bander, B.; Williams, B.M.; Al-Nuaimy, W.; Al-Taee, M.A.; Pratt, H.; Zheng, Y. Dense Fully Convolutional Segmentation of the Optic Disc and Cup in Colour Fundus for Glaucoma Diagnosis. Symmetry **2018**, 10, 87. [CrossRef]
9 Chen, X.; Xu, Y.; Wong, D.W.K.; Wong, T.Y.; Liu, J. Glaucoma detection based on deep convolutional neural network. In Proceedings of the 2015 37th Annual International Conference of the IEEE Engineering in Medicine and Biology Society (EMBC), Milan, Italy, 25–29 August 2015; Volume 2015, pp. 715–718.
10 Mary, M.C.V.S.; Rajsingh, E.B.; Naik, G.R. Retinal Fundus Image Analysis for Diagnosis of Glaucoma: A Comprehensive Survey. IEEE Access **2016**, 4, 4327–4354. [CrossRef]
11 Sinthanayothin, C. Image Analysis for Automatic Diagnosis of Diabetic Retinopathy; University of London: London, UK, 1999.
12 Krishna, B.S.; Gnanasekaran, T. Unsupervised Automated Retinal Vessel Extraction Framework Using Enhanced Filtering and Hessian Based Method with Hysteresis Thresholding. J. Med. Imaging Health Inf. **2019**, 9, 1000–1010. [CrossRef]
13 Khansari, M.M.; O'Neill, W.D.; Penn, R.D.; Blair, N.P.; Shahidi, M. Detection of Subclinical Diabetic Retinopathy by Fine Structure Analysis of Retinal Images. J. Ophthalmol. **2019**, 2019, 5171965. [CrossRef]
14 Qummar, S.; Khan, F.G.; Shah, S.; Khan, A.; Shamshirband, S.; Rehman, Z.U.; Khan, I.A.; Jadoon, W. A Deep Learning Ensemble Approach for Diabetic Retinopathy Detection. IEEE Access **2019**, 7, 150530–150539. [CrossRef]
15 Pan, X.; Jin, K.; Cao, J.; Liu, Z.; Wu, J.; You, K.; Lu, Y.; Xu, Y.; Su, Z.; Jiang, J.; et al. Multi-label classification of retinal lesions in diabetic retinopathy for automatic analysis of fundus fluorescein

angiography based on deep learning. Graefe's Arch. Clin. Exp. Ophthalmol. **2020**, 258, 779–785. [CrossRef]

16 Shankar, K.; Sait, A.R.W.; Gupta, D.; Lakshmanaprabu, S.; Khanna, A.; Pandey, H.M.; Kathiresan, S. Automated detection and classification of fundus diabetic retinopathy images using synergic deep learning model. Pattern Recognit. Lett. **2020**, 133, 210–216. [CrossRef]

17 Riaz, H.; Park, J.; Choi, H.; Kim, H.; Kim, J. Deep and Densely Connected Networks for Classification of Diabetic Retinopathy. Diagnostics **2020**, 10, 24. [CrossRef] [PubMed]

18 Agurto, C.; Murray, V.; Yu, H.; Wigdahl, J.; Pattichis, C.S.; Nemeth, S.; Barriga, E.S.; Soliz, P. A Multiscale Optimization Approach to Detect Exudates in the Macula. IEEE J. Biomed. Health Inf. **2014**, 18, 1328–1336. [CrossRef] [PubMed]

19 Rekhi, R.S.; Issac, A.; Dutta, M.K.; Travieso, C.M. Automated classification of exudates from digital fundus images. In Proceedings of the 2017 International Conference and Workshop on Bioinspired Intelligence (IWOBI), Funchal, Portugal, 10–12 July 2017; pp. 1–6.